

The Effect of Laminar Flow on Rotor Hover Performance

Austin D. Overmeyer Preston B. Martin

U.S. Army Aviation Development Directorate (ADD)
NASA Langley Research Center, Hampton, VA 23681

ABSTRACT

The topic of laminar flow effects on hover performance is introduced with respect to some historical efforts where laminar flow was either measured or attempted. An analysis method is outlined using combined blade element, momentum method coupled to an airfoil analysis method, which includes the full e^N transition model. The analysis results compared well with the measured hover performance including the measured location of transition on both the upper and lower blade surfaces. The analysis method is then used to understand the upper limits of hover efficiency as a function of disk loading. The impact of laminar flow is higher at low disk loading, but significant improvement in terms of power loading appears possible even up to high disk loading approaching 20 *psf*. A optimum planform design equation is derived for cases of zero profile drag and finite drag levels. These results are intended to be a guide for design studies and as a benchmark to compare higher fidelity analysis results. The details of the analysis method are given to enable other researchers to use the same approach for comparison to other approaches.

NOMENCLATURE

c	chord, <i>in.</i>
C_d	drag coefficient
C_l	lift coefficient
C_P	power coefficient
C_T	thrust coefficient
DL	disk loading, <i>psf</i>
F	combined root/tip loss function
FM	figure of merit
M	Mach number
N	N-factor
N_b	number of blades
PL	power loading, <i>lbs/hp</i>
r	radial coordinate, <i>in.</i>
R	rotor radius, <i>in.</i>
\bar{r}	radial station, r/R
Re	Reynolds number
V	Free-stream velocity, <i>ft/s</i>
ρ	air density, <i>slug/ft³</i>
Γ	bound circulation, <i>ft²/s</i>
λ	rotor inflow
θ	blade incidence angle, <i>deg</i>
ϕ	inflow angle, <i>deg</i>
σ	area weighted solidity

INTRODUCTION

In 1954, Powell of the National Advisory Committee for Aeronautics (NACA) completed a full-scale hover test to investigate profile power reductions with the use of natural laminar flow (NLF) airfoils, see Ref. 1. In 1966 Yaggy and Tanner, Ref. 2, measured the boundary layer transition locations on a UH-1 main and tail rotor blades using chemical sublimation. In 1974, Boatwright (Ref. 3) also used chemical sublimation to measure transition locations on a full-scale hovering rotor test stand. Both of these tests measured extensive amounts of NLF, greater than 30% chord, simultaneously on the upper and lower surface. In 2016, Richter et al., see Ref. 4, measured extensive amounts of laminar flow on the lower surface of a full-scale BK-117-type rotor in hover. Despite the measurements of NLF in hover, a significant amount of research has been focused on induced power reduction through planform variation rather than profile power reduction via NLF. In part, the limited amount of research is due to the notion that high free-stream turbulence, environmental conditions, and blade surface roughness due to manufacturing tolerances and erosion would prevent laminar flow from being achieved in flight. In addition, Prouty's 2005 Vertiflite article, Ref. 5, concluded that there is no potential for benefits of NLF in hover or cruise. This conclusion is based on the assumption that the design requirements of a supercritical airfoil to achieve laminar flow cannot be achieved while maintaining cruise performance and retreating blade stall margin.

The research performed by Powell in 1954 utilized the NACA 8-H-12 airfoil. The chart in Fig. 1 shows the predicted profile torque coefficients for three levels of surface finish/tolerance. The achievable manufacturing tolerances at that time limited the profile power reduction to only half of the theoretical predictions. Yet, a 6-7% reduction in total torque was still achieved. That translates to a 0.05 or 5 count improve-

Presented at the AHS 73rd Annual Forum, Fort Worth, Texas, May 9-11, 2017. This is a work of the U.S. Government and is not subject to copyright protection in the U.S. AMRDEC Public Release Control Number PR2874. Distribution statement A. Approved for public release.

ment in figure of merit (FM) at a disk loading of 10psf . The airfoil was predicted to achieve 40% and 80% laminar flow on the upper and lower surfaces, respectively. While the actual amount of laminar flow was not measured, the improved performance clearly indicated some amount of laminar flow was achieved.

The full-scale boundary layer transition measurements by Boatwright in 1974 were performed on an OH-23B two-bladed rotor. The rotor had only -4 degrees of linear twist using NACA0018 and NACA0012 airfoils at the root and tip, respectively. As shown in Fig. 2, a large extent of laminar flow was measured on the lower surface. Interestingly, out of the limited boundary layer measurements on rotors, most of the research has been focused on the upper surface with exception to the recent research conducted by Richter et al. In the summer of 2016, an experiment of a Mach-scale hover test was conducted in the NASA LaRC Rotor Test Cell (RTC) by the authors. Boundary layer transition locations were acquired on the upper and lower aerodynamic surfaces simultaneously via IR thermography. The hover performance was measured for natural and forced transition cases. The details of the experiment and data are given in Ref. 6.

The objective of this paper is to provide a better understanding of the effect of natural laminar flow airfoils and natural transition on hover performance. An advanced blade element momentum code was developed to predict the effects of NLF on hover performance and to predict the boundary layer transition locations. The details of the Blade Element Aerodynamics Research (BEAR) Code are presented. Next, the BEAR code predictions are compared to the experimental data set of a Mach-scale rotor in hover by the authors in Ref. 6. After comparison of the model scale data, the BEAR code is extended to full-scale to quantify the Reynolds number effects on performance and transition locations. After comparisons to experimental data, the BEAR code is used to develop theoretical hover efficiency boundaries as a function of disk loading using assumed airfoil polars. Finally, the optimum rotor hover planform is theoretically derived and a new planform design equation is presented.

THEORETICAL ANALYSIS

One of the current limitations of rotor hover analysis using comprehensive tools, such as CAMRAD or RCAS, is that either airfoil tables (C81 format) are required or CFD coupling is required. Typically, a Reynolds number correction is applied to the tables, but in some limited cases new tables are generated at the appropriate Reynolds numbers. The number of tables can grow considerably during a design cycle, especially when several airfoils are blended along the radius. The tables can allow for natural transition during the table generation; however, the information about where the boundary layer is laminar and turbulent is typically not saved. In the case of CFD coupling, the effects of natural transition are beginning to be captured with the advent of new turbulence models capable of predicting transition locations. There has been a great deal of effort to incorporate natural transition models

into CFD codes, see Refs. 7–10, but the validation of these new turbulence models is still underway. These updated CFD tools hold great promise to eventually replace the theoretical model developed for this project. While this is most certainly the path of the future, a more rapid estimation of hover performance is sometimes required during design development and assessment. As a result, a new requirement for this study on rotor blade transition was to develop a tool that could track the boundary layer state at each station and give insight into transition locations. Such a tool would need to be efficient in order to be integrated into a design sequence and a comprehensive analysis code.

In response to this requirement, a hover aerodynamic analysis code was developed to help provide insight into the boundary layer state including transition locations along the blade. Using an advanced blade element / momentum framework with all small angle approximations removed, higher order terms retained and a new root loss function, the only missing piece was to replace the C81 airfoil table lookup with a direct airfoil boundary layer analysis. The result was the BEAR code, which coupled the Blade Element Momentum Theory (BEMT) method with the PROFIL method developed by Eppler and Somers, Ref. 11. In the latest version of the PROFIL code, the boundary layer is solved using a two equation integral method coupled to an inviscid flow analysis using a panel method for low Mach number, switching to a compressibility corrected method. Then, a transonic small disturbance method was added for cases with small amounts of supersonic flow. Within the PROFIL code is the latest full e^N transition model tracking all modes of Tollmien-Schlichting instability. Crossflow and bypass transition were ignored for this first set of analysis. What made the method unique was that the airfoil analysis at each blade element station included very fine detail of low Reynolds number effects such as laminar separation bubbles and turbulent reattachment. In addition, the onset of shock induced boundary layer issues could be captured, which is important for hover at high blade loading. As a result, the Reynolds number could be changed from model to full scale, the freestream turbulence level changed, and the surface roughness could also be changed in order to study the individual effects. This has led to a tool that gives insight into scaling effects and the importance of tracking the transition location on the upper and lower blade surfaces. The analysis has no real tuning parameters except for the critical amplification ratio in the transition model, and no gridding is required.

BEAR Model

The following system of coupled nonlinear equations (derived in the Appendix) are solved using a Newton method for the inflow angle, ϕ , at each radial station, \bar{r} .

The local effective angle of attack at a blade station is a function of the incidence and the inflow angle

$$\alpha_e = \theta - \phi \quad (1)$$

In this case, the full inflow angle is defined without any small

angle approximations as

$$\tan(\phi) = \frac{\lambda}{\bar{r}} \quad (2)$$

The other important difference is that once the angle of attack, local Reynolds number and Mach number are known at a blade station, the lift and drag ($C_l = C_l(M, Re, \alpha_e)$, and $C_d = C_d(M, Re, \alpha_e)$) can be calculated with an airfoil code including the effects of natural transition. The low Reynolds number and supercritical Mach number can alter the drag coefficient to be larger than typical over portions of the blade.

After calculating the sectional lift and drag coefficients, the incremental thrust at a blade station retaining the most general form without assumptions is

$$dC_T = \frac{\sigma}{2} \lambda^2 \left[1 + \frac{1}{\tan^2 \phi} \right] [C_l \cos \phi - C_d \sin \phi] d\bar{r} \quad (3)$$

where the drag term is retained in the thrust equation and no small angle assumptions are made for the inflow angle. As shown in the Appendix, the final BEMT equation (ignoring climb rate) still includes the lift to drag ratio term, and so the BEAR hover equation is

$$\cot \phi - \frac{\sin \phi}{\bar{\phi}^2} = \frac{C_d}{C_l} \quad (4)$$

where the classical result is now a term within the new equation

$$\bar{\phi} = \sqrt{\frac{\sigma C_l}{8F\bar{r}}} \quad (5)$$

and $F = F(\bar{r}, \bar{r}_c, \phi)$ is a combined root and tip loss function (see Appendix, Eq. 72). This illustrates how the classical derivation makes some assumptions in the very beginning about the impact of drag on local thrust increment, consequentially showing no direct link between local drag and the inflow angle.

THEORETICAL RESULTS

Using the above BEAR methodology, a thrust sweep was computed where the natural transition location was calculated as a function of radius for both the upper and lower surface of the blade and compared to measurements.

Comparison with Experimental Results

Three thrust conditions of the predicted and measured transition locations are shown in Figs. 3 - 5. Note that the transition location is very sensitive to thrust and N-factor, especially when different airfoils are used along the span. The results shown here are for three N-factors, $N = 7, 11, 15$. The default value in Eppler's full e^N transition method is $N = 11$. On the lower surface, the inboard region of the RC(4)-10 airfoil shows transition moving aft over the small thrust change between Figs. 3-4, and the analysis appears to capture this process. As a result, the predicted figure of merit compares

well to the measurements in Fig. 6 for the untripped (natural transition) case using $N = 11$. For the tripped case, a very low N-factor was used, $N = 0.1$, which ensured turbulent flow on both surfaces without any device drag or impact of a trip height. It is interesting to note that at lower thrust the analysis agrees with the upper surface trip measurements, and at higher thrust the analysis agrees with the lower surface trip measurements. This is thought to be owing to the upper surface being already mostly turbulent at high thrust, and the lower surface being mostly turbulent at low thrust.

Influence of N-Factor

The only real tuning parameter that can be adjusted in the BEAR analysis is the critical amplification ratio, N . The measured data at model scale compared to analysis with two different N-factors is shown in Fig. 7. At low thrust, the $N = 15$ analysis overpredicts the FM and the $N = 7$ analysis underpredicts the FM . At higher thrust, the situation is reversed. This appears to be due to a laminar separation bubble near the root of the blade. The higher N-factor delayed transition to after laminar separation, and the lower N-factor caused earlier transition thereby preventing laminar separation.

Scale Effects

The same rotor was analyzed at two larger geometric scales to match the Reynolds numbers with a UH-60 and CH-53 size rotor, also shown in Fig. 7. The analysis shows the way in which the model scale results are predicted to scale with Reynolds number and also the critical amplification ratio, N . There are two competing factors as Reynolds number increases. Unless the airfoil design is altered, the amount of laminar flow decreases as transition moves forward with increasing Reynolds number, resulting in a drag increase. At the same time, the higher Reynolds number conditions cause the turbulent boundary layer to be reduced in height resulting in a decrease in drag. It is the second of these competing factors that is dominant for a fixed N , but both must be considered to understand how to properly scale with Reynolds number. The sensitivity to N-factor (centered around $N = 11$) appears to be as strong as the sensitivity to Reynolds number. The analysis predicts that this same rotor at CH-53 scale would be capable of FM approaching ≈ 0.82 assuming laminar flow was achieved with these same airfoils at a reasonable N .

Influence of Natural Laminar Flow on Thrust

The new theoretical approach without the classical assumptions of BEMT allows the drag to affect the local thrust and therefore also the inflow angle. A complicated interaction can then occur between the local transition movement, which changes drag and therefore inflow and angle of attack. This, in turn, changes the transition location. For a fixed collective angle, the local thrust coefficient is a function of the local drag, as shown in Fig. 8. The blue curve is for $N = 0.1$, effectively a fixed turbulent case, and the red curve is for a natural

transition case assuming $N = 11$. Coupling of the local drag and inflow results in a 2.8% increase in total thrust. In the classical approach, the sectional thrust coefficients would be identical with the absence of the coupling. A similar result is shown using CFD by Jain in Fig. 22 of Ref. 7. The low Reynolds number issues near the blade root can also setup an interaction between these terms especially in the case of very thick airfoils such as those used at the root of prop rotors.

HOVER EFFICIENCY POTENTIAL

In an effort to bound the hover performance efficiency potential that could be realized by designing for laminar flow, the BEAR code was run using two assumed airfoil polars. Here the term hover performance efficiency is defined in terms of power loading rather than figure of merit due to the common fallacy of comparing figure of merit with varying disk loading, see Chapter 5 from Leishman in Ref. 12. All the results are for an assumed standard sea-level atmosphere and a tip speed of $V_{tip} = 725 \text{ ft/s}$, $M_{tip} = 0.65$. Using an assumed series of rotor blades and the drag polars, the BEAR analysis (see Appendix) was used to study the impact of laminar flow on hover performance.

Airfoil Polar Assumption

The airfoil polars for the laminar and turbulent cases are shown in Fig. 9. The laminar airfoil was assumed to have a laminar drag bucket with a minimum drag equal to $C_d = 0.0045$ from $C_l = 0.05 - 0.70$. The turbulent airfoil drag was assumed to be a second order function of C_l with the minimum drag equal to $C_d = 0.008$ at $C_l = 0.3$. The upper and lower bounds of the laminar bucket were selected based on historical airfoil data while maintaining the low pitching moment requirement for a rotor blade airfoil. The assumption is not that a single airfoil could produce this polar, but rather a series of airfoils could be tailored to achieve the minimum drag at a given lift coefficient, Reynolds number, and Mach number. Outside of the laminar drag bucket, the drag value is equal to that of the turbulent drag polar. For comparison, the NACA 8-H-12 airfoil from the original work mentioned earlier (see Ref. 1) is shown by the red curve in Fig. 9. While these low levels of measured airfoil drag were not achieved in hover primarily due to construction techniques of that time, the polar highlights the objective of the NACA 1954 test and is very close to the polar used in the following study.

Planform Assumption

For this study, a rectangular planform was assumed with a chord to radius ratio equal to $c/R = 0.08$ yielding a solidity equal to $\sigma = 0.10$ for a four bladed rotor. The solidity was then varied by changing the number of blades in order to keep a constant chord Reynolds number for all of the cases. Finally, the twist rate was assumed to be linear from root to tip.

Comparison to Historical Studies

First, the results of the study are shown in comparison to two historical efforts to define the hovering performance efficiency potential. In 1975, Harris and McVeigh, Fig. 12 from Ref. 13, calculated the maximum figure of merit for a four bladed rotor with a variable linear twist distribution and zero profile drag. The optimum twist to minimize the induced power was calculated at each thrust level. The curve, as shown by the solid black line, was recreated in terms of power and disk loading in Fig. 10. Next, a flat plate turbulent drag coefficient as a function of Reynolds number was applied. For a $\sigma = 0.10$ and $Re_{tip} = 1.2$ and 9×10^6 , these curves are plotted by the dot-dashed and dashed black lines in Fig. 10. The following year Davis, Fig. 5 from Ref. 14, created a similar plot assuming a constant $C_l^{3/2}/C_d = 100$. This plot is also recreated in terms of disk and power loading in Fig. 10 as shown by the solid green curve. What is most interesting about the Harris/McVeigh curves is how they break over at lower disk loading. What this shows is the well known result that there is an optimum disk loading for maximum power loading of a given rotor configuration. The higher Reynolds number case (improved $C_l^{3/2}/C_d$) reaches 20% higher peak power loading than the lower Reynolds number case. It is interesting to note that this reaches the peak power loading at a slightly lower disk loading.

Theoretical Hover Efficiency Results

The results of the present study using the assumed airfoil polars and -14 degrees of linear twist rate are shown by the blue curves in Fig. 10. The curves of constant figure of merit are given in gray as a reference. At lower disk loadings, $DL \approx 4$, the high Reynolds number $Re_{tip} = 9 \times 10^6$ (turbulent) curve from Harris/McVeigh approaches the model scale laminar case. This illustrates a source of potential confusion in how model scale data with extensive laminar flow can appear similar to full scale turbulent flow data since the drag coefficients are approximately the same. In the turbulent case, the drag coefficients are lower because of the high Reynolds number. In the model scale case of the present study, the drag coefficients are low because of the laminar flow polar that was assumed. Next, in the lower Reynolds number turbulent case, the present study agrees well with the turbulent lower Reynolds number results from Harris/McVeigh.

Another practical point to consider regarding the high Reynolds number, for the Harris/McVeigh case at low disk loading, is the required rotor radius. At peak power loading, the rotor radius would have to be on the order of $R = 24 \text{ ft}$ for a four bladed rotor, which is approximately double the radius of most current helicopters in this weight class. Typically other requirements limit the rotor radius; thus, the benefits of high tip Reynolds number cannot be fully realized at lower disk loadings. However, at a fixed rotor radius and lower disk loading, significant performance improvement is possible with the use of laminar flow airfoils. As the disk loading increases (for conventional blade designs), the turbulent

and laminar curves collapse when the airfoil exits the laminar drag bucket as blade loading is increased. The assumption of a constant $C_l^{3/2}/C_d = 100$ breaks down at low disk loadings because the profile drag term approaches zero for low lift coefficients. This is also true at the root and tip of the blade for all blade loadings because the lift must equal zero at both ends of the blade (see Appendix). At high blade loadings, the profile drag term approaches a turbulent airfoil drag level. In practice, the laminar flow and natural transition effects at high disk loading become more importantly related to the maximum lift (figure of merit roll-off) of the airfoil sections due to the combination of high twist rates and tip Mach numbers (e.g., tilt rotors), but these effects are not discussed in the present study.

A study of the number of blades and linear twist rate was performed to develop a maximum hover efficiency curve for laminar airfoils analogous to the curves developed by Harris and McVeigh using the turbulent flat plate drag assumption.

The effect of blade number was developed by varying the number of blades from two to seven for all four linear twist rates. By varying blade number, the solidity is effectively varied without a change in Reynolds number. A subset of these results is shown in Fig. 11 for a single linear twist rate of $\bar{\theta} = -7^\circ$. As expected, the two bladed rotor performs the best at low disk loading due to the decrease in the profile drag term. As disk loading increases for $N_b = 2$, the power loading for the laminar case quickly approaches the turbulent case as more of the blade sections exit the laminar drag bucket. The intercept of the laminar and turbulent cases can be shifted to higher disk loadings by increasing blade number and keeping more of the blade sections in the laminar drag bucket by reducing sectional lift coefficient. In this case, significant power loading improvement is possible out to a disk loading of $DL = 20 \text{ psf}$.

Next, the effect of twist rate was studied by calculating the power loading for four twist rates $\bar{\theta} = 0^\circ, -7^\circ, -14^\circ, -21^\circ$. The results for $N_b = 4$ are shown in Fig. 12. The intercept of the laminar and turbulent cases is seen for 0° and -7° twist rates, but for the higher twist rates the intercept is at $DL > 20 \text{ psf}$. Obviously, optimizing the twist for hover can minimize the induced power term by trying to achieve uniform inflow. Alternatively, if the profile power term is minimized with a laminar flow airfoil, the increase in hover efficiency can be greater (in terms of power loading) than increasing the twist rate at some disk loadings. For example at a $DL = 10 \text{ psf}$, an untwisted laminar rotor has the potential to be more efficient than a turbulent rotor with a high twist rate, $\bar{\theta} = -21^\circ$. Since the twist rate is generally a compromise with the ideal forward flight, untwisting the rotor could have added benefits in forward flight without a hover penalty. The laminar cases show diminishing returns for increased twist rate near $DL = 12 \text{ psf}$. At this disk loading, the rotor is approaching the boundary calculated by Harris and McVeigh with $C_d = 0$ shown in Fig. 10.

By taking all of the twist rate and number of blade calculations, two curves can be developed for the maximum hover ef-

iciency. The hover efficiency potential boundaries are shown in Fig. 13 for the laminar and turbulent drag polar assumptions. The percent increase in power loading that could be realized by profile drag reduction is shown in Fig. 14. As expected, the percent increase at low disk loadings is much greater than at high disk loading because of the greater contribution of profile power to the total power. For a $DL > 10 \text{ psf}$, the percent increase is approximately a constant five percent, which is still a significant improvement in hover efficiency.

While these curves provide theoretical boundaries for laminar and turbulent rotors, the true benefits would be realized in a full system study. By increasing the design space with an assumed laminar drag polar (i.e., airfoil family), the aircraft designer might find a different optimal design for a given mission profile. For example, the increase in hover efficiency could be traded for added fuel for mission range, or the twist could be reduced to increase forward flight speed at the same hover efficiency. Ultimately, higher fidelity tools and experimental tests are required to validate any new design, but these theoretical boundaries can be used as a benchmark for concept designs.

OPTIMUM HOVER PLANFORM

After defining the theoretical bounds of hover efficiency in the previous section, the BEAR equations are reexamined to better understand how an optimum hovering rotor could be designed in practice.

Approximation of Method

First, an approximation of the method is developed to obtain a closed formed solution of the BEAR equation. By neglecting climb rate and assuming $C_d = 0$, Eq. 4 reduces to

$$\bar{\phi}^2 = \tan \phi \sin \phi \quad (6)$$

and the trigonometric terms can be approximated by a third order Maclaurin series approximation such that

$$\bar{\phi}^2 = \phi^2 + \frac{\phi^4}{6} - \frac{\phi^6}{18} \quad (7)$$

The resulting approximate (indicated by the * superscript) closed form solution after neglecting the sixth order terms in ϕ^* is

$$\phi^* = \sqrt{\sqrt{6\bar{\phi} + 9} - 3} \quad (8)$$

which again is a function of the classical solution $\bar{\phi}$ given by Eq. 5. Had the fourth order terms also been neglected, then the result collapses identically to the classical theory

$$\phi^* = \bar{\phi} \quad (9)$$

If the fourth order terms are retained, the result for ϕ^* can be integrated to explore the maximum predicted figure of merit for the assumptions of $C_d = 0$ and neglecting only sixth order

terms in ϕ^* . Assuming the inflow is given by the Maclaurin series for the tangent function as

$$\lambda^* = \left(\phi^* + \frac{(\phi^*)^3}{3} \right) \bar{r} \quad (10)$$

the incremental thrust and torque can be integrated using momentum theory for both thrust

$$C_T = \int_0^1 4\lambda^2 \bar{r} d\bar{r} \quad (11)$$

and induced power (since $C_d = 0$) required.

$$C_P = \int_0^1 4\lambda^3 \bar{r} d\bar{r} \quad (12)$$

As a result, an ideal figure of merit can be calculated as a theoretical upper bound for the case using the small angle approximations where $\lambda = \bar{\lambda} = \bar{\phi} \bar{r}$ and also for the case only ignoring sixth order terms where $\lambda = \lambda^*$ in the integrals leading to the figure of merit.

$$FM = \frac{1}{\sqrt{2}} \frac{C_T^{3/2}}{C_P} \quad (13)$$

For the assumption that the term $\sigma C_l / F$ remains equal to a constant for all radial stations, the maximum possible figure of merit with $C_d = 0$ is computed for the small angle case to be

$$FM = 0.953 \quad (\lambda = \bar{\lambda}) \quad (14)$$

and for the series approximated (only sixth order terms neglected) BEAR case to be

$$FM = 0.920 \quad (\lambda = \lambda^*) \quad (15)$$

which agrees with the Harris-McVeigh solution at nominal disk loading ($DL = 10 \text{ psf}$) with $C_d = 0$ shown in Fig. 10.

Required Loading for Uniform Inflow

The last section required $\sigma C_l / F$ to be a constant leading to nonuniform inflow. One other interesting result is to derive the radial loading required to achieve uniform inflow. As an example, the ideal case of constant inflow, $\bar{\lambda}$ is considered using the full inflow equation.

$$\tan \phi = \frac{\bar{\lambda}}{\bar{r}} \quad (16)$$

Substituting this result into the original BEAR equation, Eq. 4, without approximation gives

$$\bar{\phi}^2 = \frac{\sin \left(\tan^{-1} \left(\frac{\bar{\lambda}}{\bar{r}} \right) \right)}{\frac{\bar{r}}{\bar{\lambda}} - \frac{C_d}{C_l}} \quad (17)$$

Using the definition of $\bar{\phi}$ from Eq. 5, the taper and/or twist required for uniform inflow must vary as

$$\sigma C_l = 8F \bar{r} \frac{\sin \left(\tan^{-1} \left(\frac{\bar{\lambda}}{\bar{r}} \right) \right)}{\frac{\bar{r}}{\bar{\lambda}} - \frac{C_d}{C_l}} \quad (18)$$

and using the identity

$$\sin \left(\tan^{-1} x \right) = \frac{x}{\sqrt{1+x^2}} \quad (19)$$

Eq. 18 reduces to

$$\sigma C_l = 8F \frac{1}{\left(1 - \frac{C_d}{C_l} \frac{\bar{\lambda}}{\bar{r}} \right)} \frac{\left(\frac{\bar{\lambda}}{\bar{r}} \right)^2}{\sqrt{1 + \left(\frac{\bar{\lambda}}{\bar{r}} \right)^2}} \quad (20)$$

This fundamental result shows $\sigma C_l \sim F / \bar{r}$ will be compared to other approaches for deriving the optimum planform in the next two sections.

Ideal Bound Circulation Distribution, $C_d = 0$

Neglecting drag, the local bound circulation at a blade element can be found by equating the two definitions of net thrust force at a blade element perpendicular to the rotational velocity

$$\rho (\Omega \bar{r}) \Gamma = \frac{1}{2} \rho (\Omega \bar{r})^2 c C_l \cos \phi \quad (21)$$

and after non-dimensionalizing.

$$\bar{\Gamma} = \frac{N_b \Gamma}{\pi \Omega R^2} = \frac{\sigma C_l \bar{r}}{2} (\cos \phi) \quad (22)$$

Solving the BEAR equation, for the case of $C_d = 0$ (Eq. 6), for the local loading yields

$$\sigma C_l = 8F \bar{r} \frac{\sin^2 \phi}{\cos \phi} \quad (23)$$

Substituting this into Eq. 22 gives an expression for the circulation distribution.

$$\bar{\Gamma} = 4F \bar{r}^2 \sin^2 \phi \quad (24)$$

Performing the same derivation in the far wake using the propeller based method outlined by Adkins and Liebeck, Ref. 15, results in an identical equation for the hovering rotor circulation distribution using their Fig. 2 and its description.

Assuming uniform inflow, the ideal circulation can be expanded into

$$\bar{\Gamma}_i = 4F \bar{r}^2 \sin^2 \left(\tan^{-1} \left(\frac{\bar{\lambda}}{\bar{r}} \right) \right) \quad (25)$$

and using the identity

$$\sin^2 \left(\tan^{-1} x \right) = \frac{x^2}{1+x^2} \quad (26)$$

the circulation reduces to

$$\bar{\Gamma}_i = 4F \bar{\lambda}^2 \left(\frac{\bar{r}^2}{\bar{\lambda}^2 + \bar{r}^2} \right) \quad (27)$$

where the result is a circulation distribution that is in the same form as published by Glauert (Ref. 16) as $x^2/(1+x^2)$ for a propeller with the term $x = \bar{r}/\bar{\lambda}$ instead of the propeller definition of $x = \bar{r}/V$.

Optimum Planform, $C_d \neq 0$

The result for the ideal circulation distribution (Eq. 27) is a good starting point for a planform design, but this assumes zero profile drag. To design the optimum planform, the profile drag term must be retained. Again, starting with the propeller design method outlined by Glauert (Ref. 16) and Theodorsen (Ref. 17), the planform can be modified based on the airfoil characteristics. Beginning with the blade element definitions (see Appendix Eqs. 38-39) and using the full inflow equation, Eq. 2, the local thrust and power increment at a radial station, \bar{r} , reduces to

$$C'_T = dC_T = \frac{\sigma C_l}{2 \cos \phi} \bar{r}^2 \left[1 - \frac{C_d}{C_l} \tan \phi \right] d\bar{r} \quad (28)$$

$$C'_P = dC_P = \frac{\sigma C_l}{2 \cos \phi} \bar{r}^3 \left[\tan \phi + \frac{C_d}{C_l} \right] d\bar{r} \quad (29)$$

Next, Glauert and Theodorsen describe the efficiency of each radial station as the work divided by the consumed power. Therefore, the efficiency for a radial station can be defined by

$$\eta = \frac{\lambda C'_T}{C'_P} = \frac{\left[\tan \phi - \frac{C_d}{C_l} \tan^2 \phi \right]}{\left[\tan \phi + \frac{C_d}{C_l} \right]} \quad (30)$$

The optimum design of a radial station is achieved by maximizing the efficiency as a function of bound circulation, thus the optimum is calculated as

$$\frac{\partial \eta}{\partial \Gamma} = 0 \quad (31)$$

The inflow angle, drag coefficient and lift coefficient in Eqn. 30 are functions of the bound circulation such that the partial derivative in Eqn. 31 cannot easily be calculated analytically. Alternatively, the optimum planform can be derived numerically using an iterative method within the BEAR code. The designer could elect to optimize the planform through twist and/or taper.

As a simple example, a fixed twist rate of $\theta \bar{r} = -14^\circ$ was selected and a planform was optimized using only taper. First, the taper was optimized using the turbulent drag polar assumption from Fig. 9. At each radial station, the bound circulation was increased by adding solidity. The full BEAR equations were solved for varying solidity to account for the sensitivities of drag, lift and inflow angle to bound circulation. By satisfying Eq. 31, the optimum solidity for every radial station was calculated as shown by the chord distribution with the blue curve in Fig. 15. The same approach was performed using the laminar drag polar assumption, Fig. 9. The optimized laminar planform is shown by the red curve in Fig. 15, compared to the turbulent optimized planform for the same disk loading of $DL = 10 \text{ psf}$. The increased airfoil efficiency of NLF allows the mid-span of the blade to operate at a higher lift coefficients by removing solidity. Therefore, the decrease in profile power is not only due to the reduction in profile drag, but also the reduction in solidity. This is shown

by comparing the optimized turbulent and laminar columns of Table 1. The last column is the theoretical performance of the planform optimized for the turbulent airfoil polar but with the laminar airfoil drag polar. This shows that the full performance benefits of NLF airfoils cannot be realized by simply replacing turbulent airfoils on an existing planform.

The next step would be to replace the assumed airfoil polars with a direct airfoil boundary layer analysis. The planform optimization routine coupled to airfoil analysis would also allow the bound circulation sensitivities to Reynolds number, Mach number and transition locations to be captured. For example, near the blade root, excessive taper can aggravate low Reynolds number issues such as the formation of laminar separation bubbles. The result would be a new optimum planform shape, then the one presented in Fig. 15, based on the airfoil performance characteristics.

CONCLUSIONS

This study compared new, high-quality hover measurements on a modern advanced rotor to predictions using a relatively simple analysis tool in order to highlight the importance of laminar flow and natural transition effects on hover. Several important conclusions were drawn from this work.

1. Laminar flow has existed on rotor blades at all scales since the very beginning of helicopter flight; however, the effects of laminar flow (i.e., natural transition) have remained poorly understood and under appreciated until recently.
2. Without the small angle assumptions used in classical BEMT, the theoretical maximum figure of merit was shown to be equal to, $FM = 0.920$ with zero profile drag, $C_d = 0$. The ideal taper and/or twist distributions become a strong function of the root/tip loss function and the local airfoil lift to drag ratio, with the bound circulation rolling off to zero near the root and tip.
3. High quality hover performance measurements have been acquired along with the measurement of the local boundary layer transition location. These measurements indicate that hover performance at model scale is a strong function of the amount of laminar flow, and analysis prediction methods must include natural transition models in order to understand scaling model data to flight Reynolds numbers.
4. The e^N transition model running within a combined blade element momentum analysis tracked the movement of transition very well for most of the blade over a range of thrust levels. This model assumes the mechanism for transition on the rotor blade is dominated in hover by Tollmien-Schlichting waves, but this has not been proven in this work. More work is required to better understand the mechanisms and receptivity of boundary layers in a rotating environment.

5. The bounds of the hover efficiency are defined with assumed laminar and turbulent airfoil polars. For disk loadings up to, $DL \approx 12 \text{ psf}$, an untwisted rotor with natural laminar flow airfoils can theoretically achieve the same hover efficiency as a high linear twist rate (-21°) rotor with turbulent airfoils.
6. The optimum planform for a given thrust is a function of the profile drag, thus the airfoil design can alter the optimum planform. The planform design process must be coupled to the airfoil design.

ACKNOWLEDGMENTS

The dedicated work of the test team and NASA Langley staff were greatly appreciated. The personal communications and encouragement from Tony McVeigh (Boeing) on the BEAR equations were greatly appreciated and was the impetus for much of this work. The encouragement from Prof. Mark Maughmer (Penn State University) on research into the importance of laminar flow effects despite the earlier opposition of a majority of the community was also very important to this work.

REFERENCES

- ¹Powell, Jr., R., "Hovering Performance of Helicopter Rotor Using NACA 8-H-12 Airfoil Sections," *NASA TN-3237*, 1954.
- ²Tanner, W. and Yaggy, P., "Experimental Boundary Layer Study on Hovering Rotors," *Journal of the American Helicopter Society*, Vol. 11, 1966, pp. 22–37.
- ³Boatwright, D., "Three-Dimensional Measurements of the Velocity in the Near FLOW Field of a Full-Scale Hovering Rotor," *AD-781-547*, 1974.
- ⁴Richter, K., Schulein, E., Ewers, B., Raddatz, J., and Klein, A., "Boundary Layer Transition Characteristics of a Full-Scale Helicopter Rotor in Hover," *American Helicopter Society 72nd Annual Forum*, West Palm Beach, FL, May 17-19 2016.
- ⁵Prouty, R., "Airfoil Choices," *Vertiflite*, Vol. 51, No. 2, Summer 2005, pp. 14–15.
- ⁶Overmeyer, A. and Martin, P., "Measured Boundary Layer Transition and Hover Performance at Model Scale," *55th AIAA Aerospace Sciences Meeting*, Grapevine, TX, January 2017, AIAA 2017-1872.
- ⁷Rohit, J., "CFD Performance and Turbulence Transition Predictions on an Installed Model-scale Rotor in Hover," *55th AIAA Aerospace Sciences Meeting*, Grapevine, TX, January 2017, AIAA 2017-1871.
- ⁸Heister, C. C., "Laminar-Turbulent Transition Prediction for Helicopter Rotors in Hover and Forward Flight - a RANS Based Investigation of Transition Mechanisms Using Empirical Criteria," *38th European Rotorcraft Forum*, Amsterdam, Netherlands, Sept. 2012.
- ⁹Coder, J., "Enhancement of the Amplification Factor Transport Transition Modeling Framework," *55th AIAA Aerospace Sciences Meeting*, Grapevine, TX, January 2017, AIAA 2017-1709.
- ¹⁰Vieira, B. A., Kinzel, M., and Maughmer, M. D., "CFD Hover Predictions Including Boundary-Layer Transition," *55th AIAA Aerospace Sciences Meeting*, Grapevine, TX, January 2017, AIAA 2017-1665.
- ¹¹Eppler, R. and Somers, D. M., "A Computer Program for the Design and Analysis of Low-Speed Airfoils," *NASA TM-80210*, Langley Research Center, August 1980.
- ¹²Leishman, J. G., *The Helicopter Thinking Forward Looking Back*, College Park Press, College Park, MD, 2007, pp. 42–64.
- ¹³Harris, F. and McVeigh, M., "Uniform Downwash with Rotors having a finite number of blades," *American Helicopter Society Symposium on Helicopter Aerodynamic Efficiency*, March 6-7 1975.
- ¹⁴Davis, S., "Research Requirements for Development of Improved Helicopter Rotor Efficiency," *NASA CR-145117*, 1976.
- ¹⁵Adkins, C. and Liebeck, R., "Design of Optimum Propellers," *Journal of Propulsion and Power*, Vol. 10, No. 5, Sept-Oct 1994.
- ¹⁶Glauert, H., *Airplane Propellers*, Vol. 4, Div. L, Sec. 4, Julius Springer-Verlag, Berlin, 1935, Durand, W.F. ed. Aerodynamic Theory, Reprinted 1963 by Dover Publications, New York, pp. 236–269.
- ¹⁷Theodorsen, T., "The Theory of Propellers. IV- Thrust Energy, and Efficiency Formulas for Single- and Dual-Rotating Propellers with Ideal Circulation Distribution," 1944, NACA Rep. 778.
- ¹⁸Leishman, J. G., *Principles of Helicopter Aerodynamics*, Cambridge University Press, New York, NY, 2000, pp. 568–572.

PROFILE TORQUE CURVES OF NACA 8-H-12 ROTOR BLADES

$\Omega R = 455 \text{ FPS}$; $\sigma = 0.041$

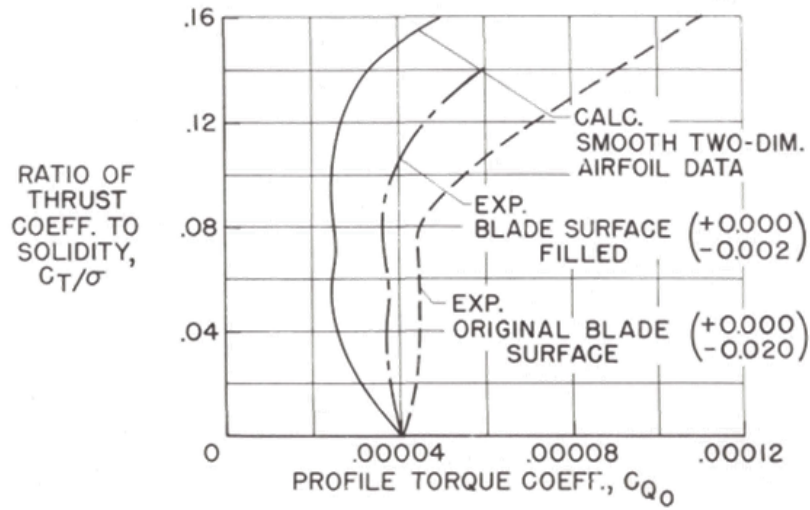


Fig. 1: Predicted and experimental profile torque with varying surface finish from NACA full-scale test (1954), Ref. 1.

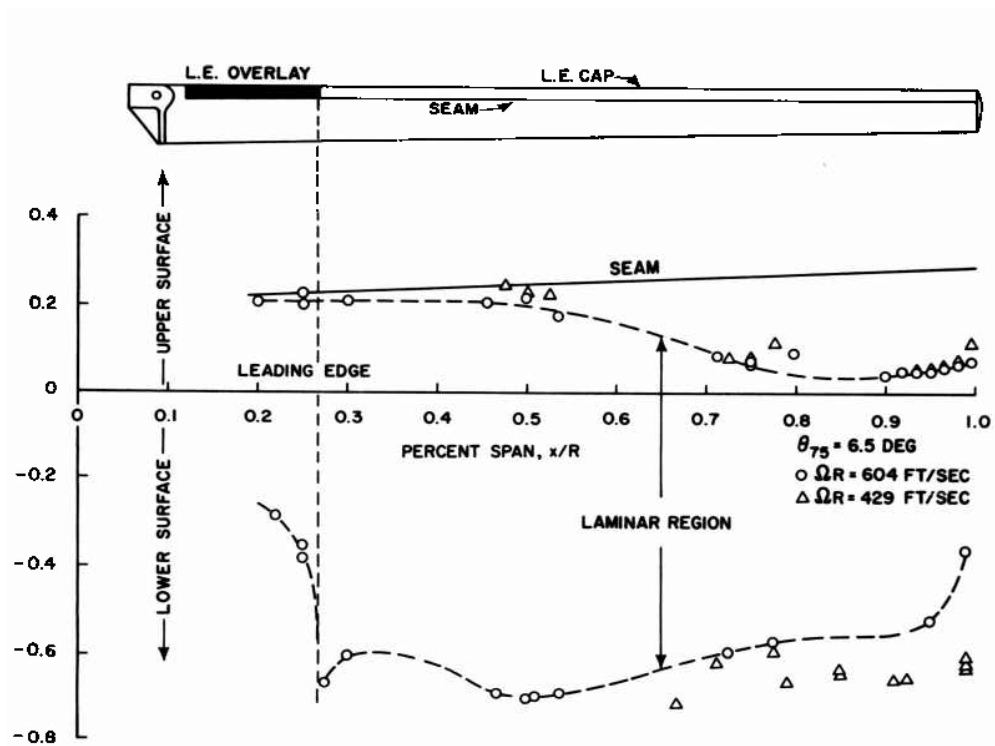


Fig. 2: Measured Transition Locations on a Full-Scale Hovering Rotor, $C_T/\sigma = 0.050$, Ref. 3.

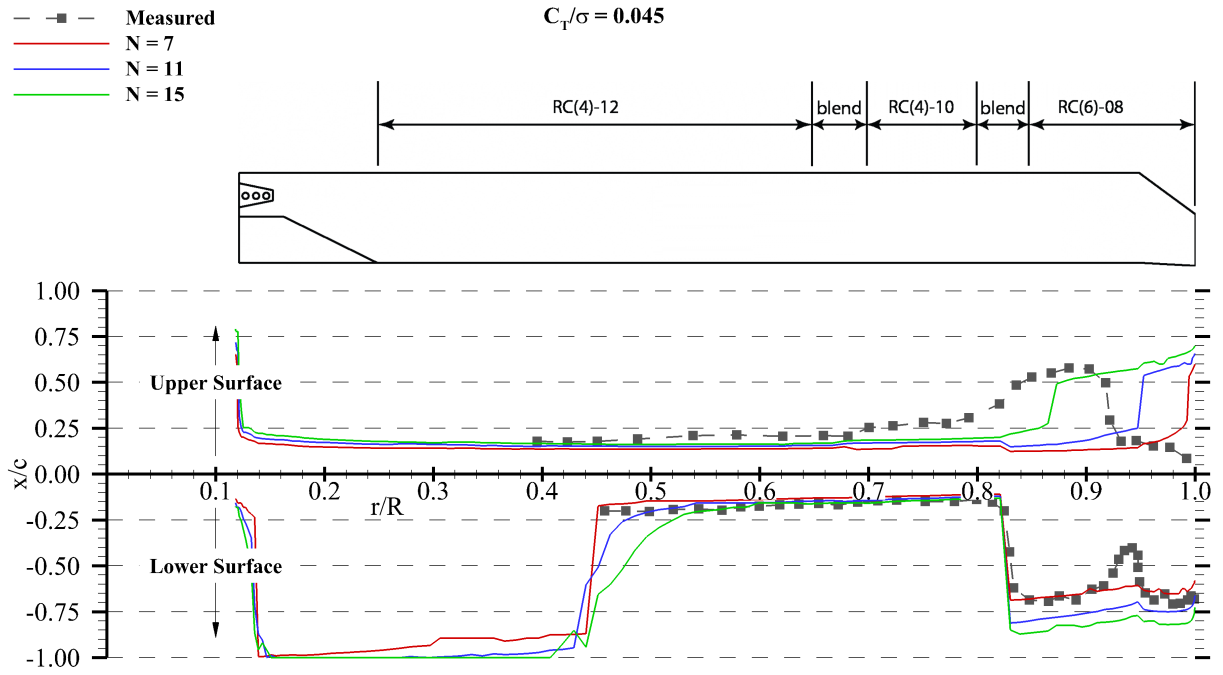


Fig. 3: Comparison of experimental and predicted transition locations for varying N-factor, $C_T/\sigma = 0.045$.

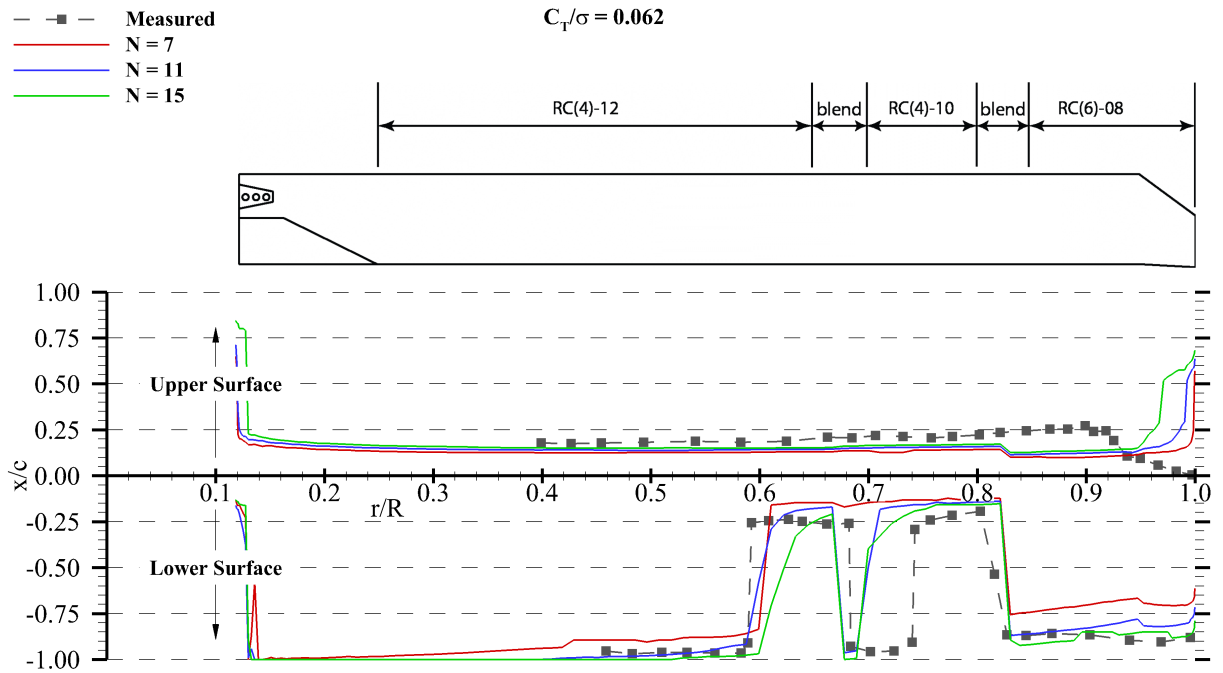


Fig. 4: Comparison of experimental and predicted transition locations for varying N-factor, $C_T/\sigma = 0.062$.

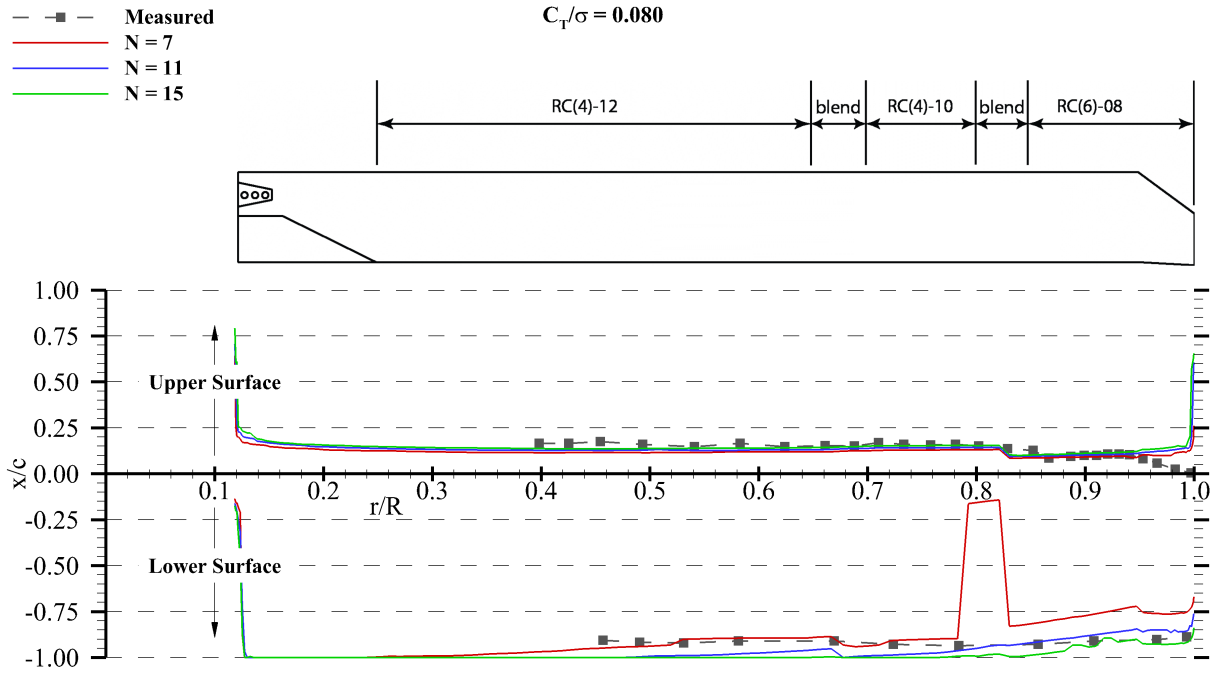


Fig. 5: Comparison of experimental and predicted transition locations for varying N-factor, $C_T/\sigma = 0.080$.

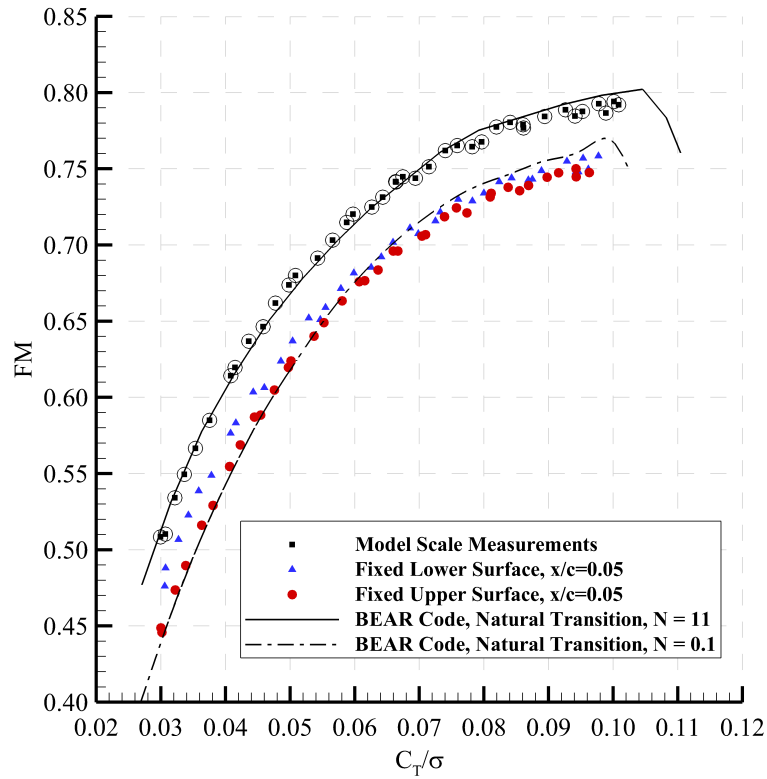


Fig. 6: Effect of N-Factor on hover performance prediction and comparison to experimental data.

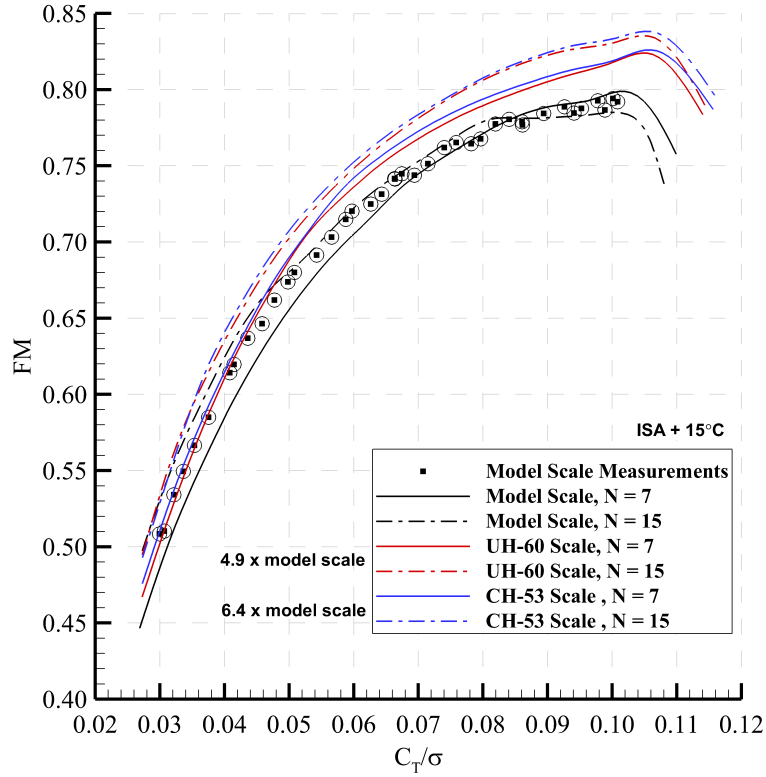


Fig. 7: Effect of scale on hover performance.

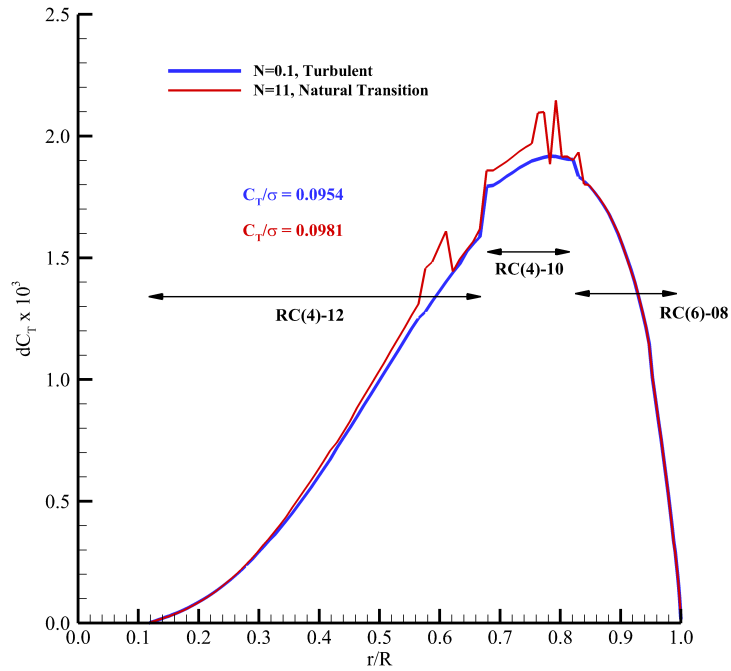


Fig. 8: Effect of natural laminar flow on sectional thrust coefficient.

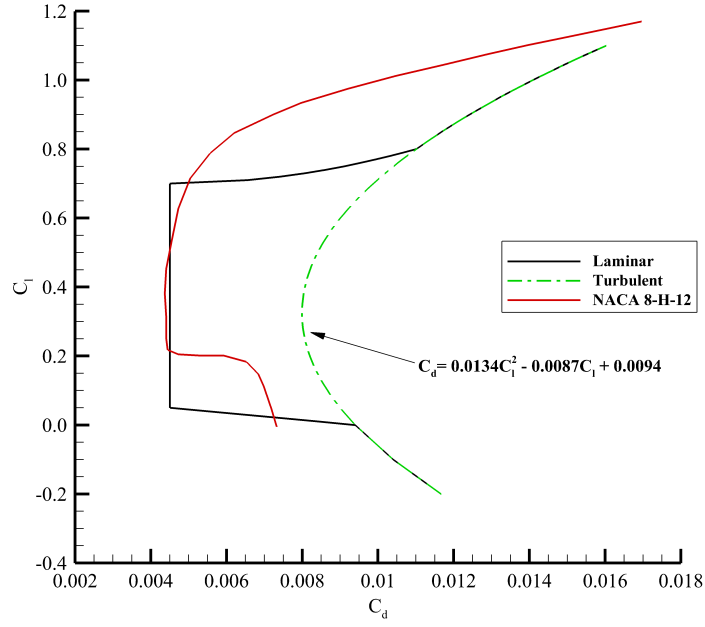


Fig. 9: Assumed airfoil drag polars for laminar and turbulent airfoils.

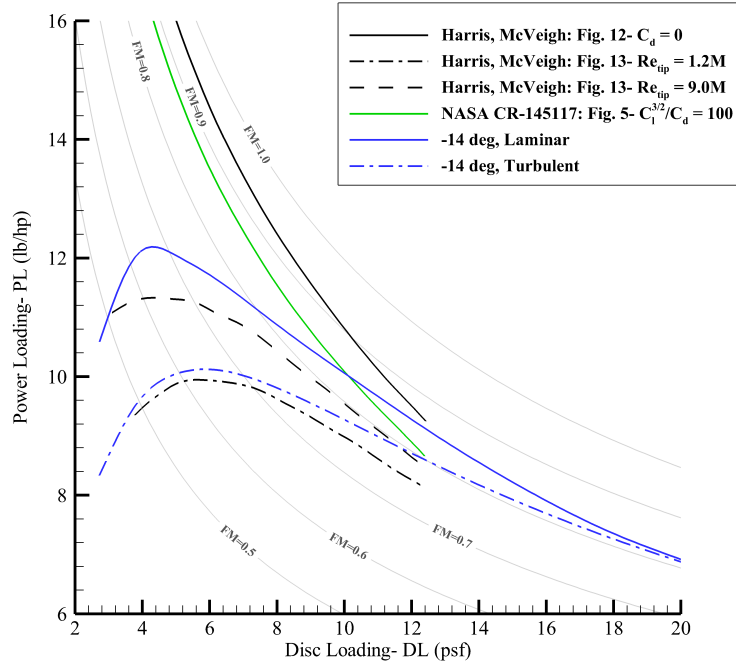


Fig. 10: Comparison to historical hover efficiency potential: $V_{tip} = 725 \text{ ft/s}$, $N_b = 4$.

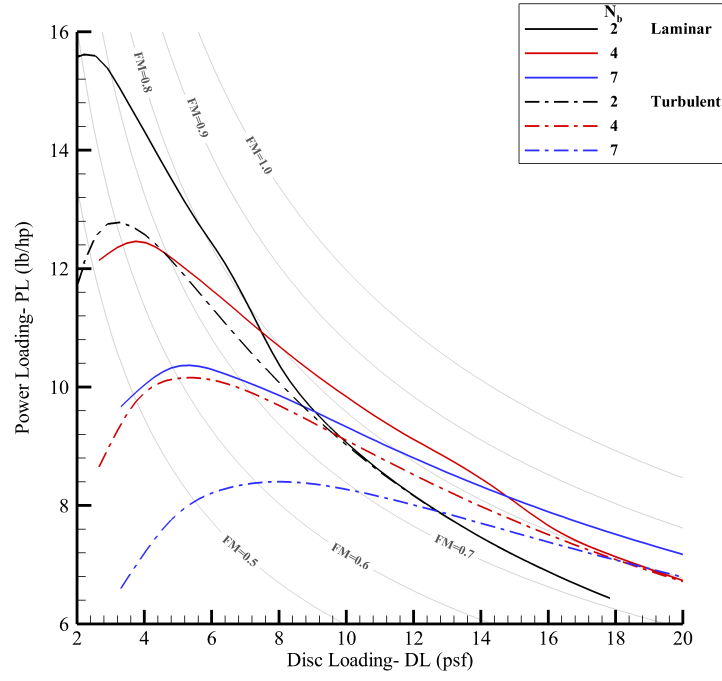


Fig. 11: The effect of number of blades on hover efficiency potential: $V_{tip} = 725 \text{ ft/s}$, $\theta \bar{r} = -7^\circ$.

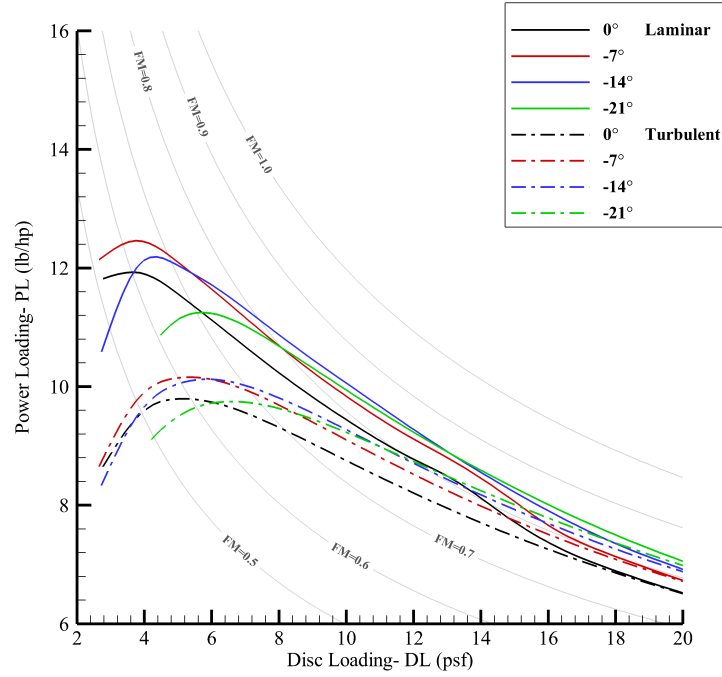


Fig. 12: The effect of twist rate on hover efficiency potential: $V_{tip} = 725 \text{ ft/s}$, $NB = 4$.

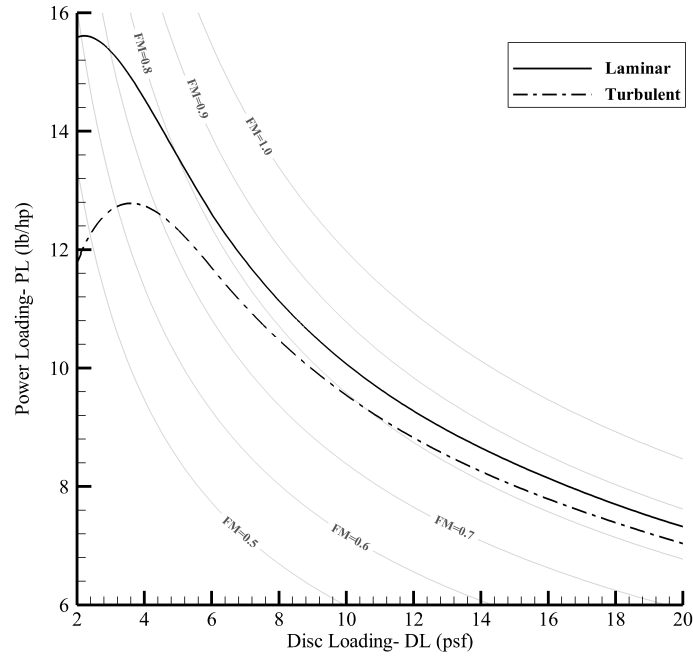


Fig. 13: Comparison of laminar and turbulent airfoil drag on the hover efficiency potential: $V_{tip} = 725 ft/s$.

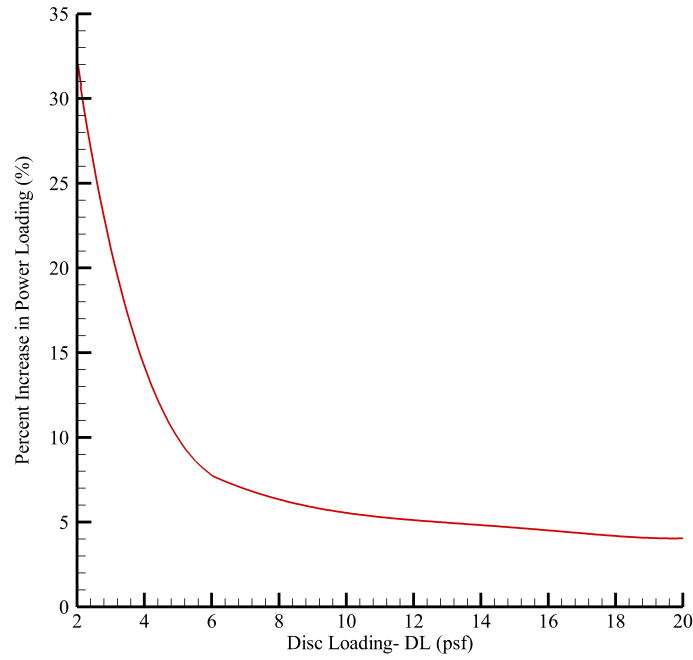


Fig. 14: Potential percent increase in power loading versus disc loading: $V_{tip} = 725 ft/s$.

Table 1: Performance comparison of optimized planform.

Parameter	Optimized Turbulent	Optimized Laminar	Optimized Turbulent (Laminar Drag)
FM	0.779	0.859	0.839
PL	9.3	10.3	10.1
σ	0.106	0.087	0.106
$C_P \times 10^3$	0.651	0.589	0.602
$C_{P,i} \times 10^3$	0.548	0.542	0.546
$C_{P,o} \times 10^3$	0.103	0.047	0.056

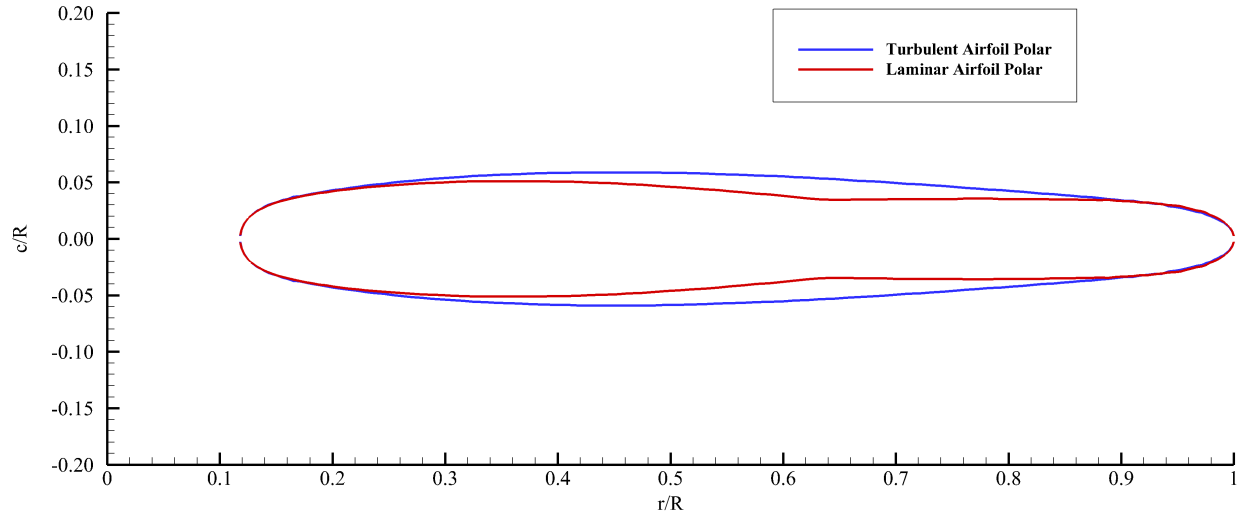


Fig. 15: Comparison of the optimum planform using a turbulent and laminar drag polar assumption: $DL = 10 \text{ psf}$, $\theta\bar{r} = -14^\circ$.

APPENDIX

The blade planform is divided into spanwise stations with each viewed as 2D airfoil sections. For each station, the local incremental thrust is derived using first blade element theory and then again using momentum theory. The results of the two derivations are then set equal to develop a combined blade element momentum theory (BEMT) solution.

Blade Element Theory

At each airfoil station, the effective angle of attack is defined as the induced inflow angle subtracted from the local blade pitch angle including collective and geometric twist as

$$\alpha_e = \theta - \phi \quad (32)$$

The incremental thrust at a blade station retaining the most general form without assumptions is

$$dT = \frac{1}{2} \rho N_b c W^2 [C_l \cos(\phi) - C_d \sin(\phi)] dr \quad (33)$$

which after nondimensionalization by

$$dC_T = \frac{dT}{\rho (\Omega R)^2 \pi R^2} \quad (34)$$

the incremental thrust coefficient is then

$$dC_T = \frac{\sigma}{2} \frac{W^2}{(\Omega R)^2} [C_l \cos(\phi) - C_d \sin(\phi)] d\bar{r} \quad (35)$$

The full inflow angle is defined without any small angle approximations as

$$\tan(\phi) = \frac{\lambda}{\bar{r}} \quad (36)$$

The incident velocity at a blade station is then a function of both the inflow and blade rotation

$$\frac{W^2}{(\Omega R)^2} = \frac{u^2 + (\Omega r)^2}{(\Omega R)^2} = \lambda^2 + \bar{r}^2 \quad (37)$$

After substitution of the inflow angle definition and the incident velocity, the local thrust increment from blade element theory is

$$dC_T = \frac{\sigma}{2} \lambda^2 \left[1 + \frac{1}{\tan^2 \phi} \right] [C_l \cos \phi - C_d \sin \phi] d\bar{r} \quad (38)$$

Similarly, the local power increment is

$$dC_P = \frac{\sigma}{2} \lambda^2 \bar{r} \left[1 + \frac{1}{\tan^2 \phi} \right] [C_l \sin \phi + C_d \cos \phi] d\bar{r} \quad (39)$$

Momentum Theory

The derivation of ‘‘General Momentum Theory’’ by Glauert (Ref. 16) is repeated with only slight nomenclature modification and including the root/tip loss function F , climb rate V_c ,

and the slipstream contraction ratio $\frac{S}{S_1}$. The incremental thrust from momentum theory is

$$dT = \rho u (u - V_c) 2\pi r \left(\frac{S}{S_1} \right) F dr \quad (40)$$

After nondimensionalization as before, the incremental thrust coefficient defined by momentum theory is

$$dC_T = \frac{\rho u (u - V_c) 2\pi r \left(\frac{S}{S_1} \right) F dr}{\rho (\Omega R)^2 \pi R^2} \quad (41)$$

Assuming a fully contracted rotor $\frac{S}{S_1} = 2$.

$$dC_T = 4 [\lambda^2 - \lambda \lambda_c] F \bar{r} d\bar{r} \quad (42)$$

Combined BEMT

By combining the results of both blade element theory and momentum theory, an equation for the inflow angle can be derived as

$$\frac{\sigma}{2} \lambda^2 \left[1 + \frac{1}{\tan^2 \phi} \right] [C_l \cos \phi - C_d \sin \phi] d\bar{r} = 4 [\lambda^2 - \lambda \lambda_c] F \bar{r} d\bar{r} \quad (43)$$

Or in terms of the inflow angle, the equation is

$$\left(\frac{8F}{\sigma C_l} \right) \frac{1}{\cos \phi} \left[\frac{\bar{r} \tan \phi - \lambda_c}{1 + \tan^2 \phi} \right] + \frac{C_d}{C_l} = \frac{1}{\tan \phi} \quad (44)$$

and upon using the trigonometric identity for $1 + \tan^2 \phi = \sec^2 \phi$

$$\left(\frac{8F}{\sigma C_l} \right) \cos \phi [\bar{r} \tan \phi - \lambda_c] + \frac{C_d}{C_l} = \frac{1}{\tan \phi} \quad (45)$$

and rearranging terms

$$\left(\frac{8F}{\sigma C_l} \right) [\bar{r} \sin \phi - \lambda_c \cos \phi] + \frac{C_d}{C_l} = \cot \phi \quad (46)$$

This is the fundamental equation within the BEAR analysis with the root/tip loss function given by Eq. 72. If the climb velocity is neglected for the pure hover case (as is the topic of this paper), the equation reduces to

$$\left(\frac{8F \bar{r}}{\sigma C_l} \right) \sin \phi + \frac{C_d}{C_l} = \cot \phi \quad (47)$$

Comparison to Classical Result

It very important to anchor any new equation to that of the well known classical theory (e.g., Ref. 18). To begin, if a small angle assumption were made for ϕ at the beginning of the derivation as in the case of the classical analysis (Ref. 18), then Eq. 47 reduces to

$$\left(\frac{8F \bar{r}}{\sigma C_l} \right) (\phi) + \frac{C_d}{C_l} = \frac{1}{\phi} \quad (48)$$

which can be formed into a quadratic equation

$$\left(\frac{8F\bar{r}}{\sigma C_l}\right)(\phi^2) + \frac{C_d}{C_l}(\phi) = 1 \quad (49)$$

and solved for ϕ subject to the small angle approximation

$$\phi = \frac{-\sigma C_l}{16F\bar{r}} \left[\frac{C_d}{C_l} - \sqrt{\left(\frac{C_d}{C_l}\right)^2 + \left(\frac{32F\bar{r}}{\sigma C_l}\right)} \right] \quad (50)$$

upon isolating the drag terms by multiplying through by the lift coefficient

$$\phi = \frac{-\sigma}{16F\bar{r}} \left[C_d - \sqrt{C_d^2 + \left(\frac{32FC_l\bar{r}}{\sigma}\right)} \right] \quad (51)$$

such that the assumption can now be made for zero profile drag $C_d = 0$, and the solution for the inflow angle becomes the classical result

$$\bar{\phi} = \sqrt{\frac{\sigma C_l}{8F\bar{r}}} \quad (52)$$

This same result can also be derived in the classical theory by combining equations 3.15 and 3.47 of Ref. 18 and solving for $\bar{\phi}$. As a result, the original full hover BEAR equation (Eq. 47) without any small angle assumptions and with nonzero profile drag can be written as

$$\cot \phi - \frac{\sin \phi}{\bar{\phi}^2} = \frac{C_d}{C_l} \quad (53)$$

where the classical result (defined by Eq. 52) is now a term in the new equation giving a modified inflow angle. This is the form used in the body of the text.

This equation can also be written in a more convenient form used within the BEAR code Newton solver

$$\tan \phi = \frac{C_l}{C_d} - \frac{T_1}{T_2} \quad (54)$$

where

$$T_1 = 8F\bar{r} \tan^2 \phi \quad (55)$$

and

$$T_2 = \sigma C_d (1 + \tan^2 \phi) \cos \phi \quad (56)$$

TIP AND ROOT LOSS FUNCTION

There are many methods to account for tip loss or more specifically the effect of a finite number of blades. There are fewer methods that account for the bound circulation going to zero near the root of the blade. As a result, in 2003 it was desired to develop an improved combined root/tip loss method based on the original model developed by Prandtl as described in Durand, Ref. 16. Similar to the Trefftz plane analysis in fixed wing aerodynamics, this method is derived in the far wake. The far wake model is a linear superposition of four vertically infinite columns of vortex sheets (see Fig. 16), where each vortex sheet within a column is semi-infinite in the spanwise

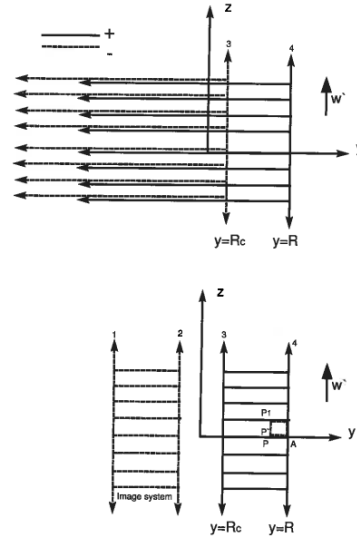


Fig. 16: Theoretical model of far wake vortex sheet structure.

direction. The original Prandtl tip loss model used only a single column with the spanwise termination at the outer edge of the wake. Inboard, the vortex sheets were infinite and so superposition of an opposite sign stack of vortex sheets terminating at the root cutout (see Fig. 16) allowed for a combined result to have a root and tip loss effect. The fact that the original model was semi-infinite in the spanwise direction toward the root did not affect the results required for the tip area. Since this new model attempts to include both the root and tip loss effects, it was determined that two columns were required for the root and tip of the blade, and two more were required for the image system reflected across the z-axis. By partially canceling, these four columns then combine to mathematically approximate the presence of the physical columns extending from $y = -R_c$ to $y = -R$ and $y = R_c$ to $y = R$ as shown in Fig. 16. Following the same method as Prandtl, the boundary conditions of zero loading at the root and tip are used to finally solve for the combined root/tip loss function.

Derivation of Combined Root/Tip Loss Function

As shown in the original derivation (Ref. 16), the first step in the process is to integrate the vertical velocity distribution between two of the neighboring vortex sheets. For example, the velocity distribution from point P' to P_1 in Fig. 16 could be integrated over the sheet spacing, s , to find an average value as

$$\bar{w} = \frac{1}{s} \int_0^s w \, dz \quad (57)$$

Away from the ends of the sheet, there should be no vertical velocity and $\bar{w} = 0$. Near the edges of the sheets, the vertical streamlines become curved inboard near the tip area and outboard near the root area due to the effects of the finite ends of the vortex sheets. In both cases, this results in a non-zero vertical velocity. At the very edge of the sheets, the mean velocity approaches that of the rate of descent, w' , of the column of vortex sheets. As a result the combined loss function, F ,

is just a function of the development of this non-zero vertical velocity between two subsequent vortex sheets

$$w' - \bar{w} = F w' \quad (58)$$

The elegance of the original derivation is in the proof that the vertical velocity integral for \bar{w} can be written as a function of the velocity potential increase from point P to point A such that the tip loss function is then

$$F = \frac{2}{w's} \Phi(PA) \quad (59)$$

here this new method deviates from the original derivation is that this potential function is now a superposition of four different columns of vortex sheets instead of a single column

$$\Phi(PA) = k_1\Phi_1 + k_2\Phi_2 + k_3\Phi_3 + k_4\Phi_4 \quad (60)$$

where the influence coefficients, k_n , are determined by the boundary conditions for zero loading at the root and tip. The definition of the velocity potential for each of the sheets is identical in form (Ref. 16)

$$\Phi_n(PA) = w' \int_{-a}^{+a} \frac{e^{\pi(y+c_n)/s}}{\sqrt{1 - e^{2\pi(y+c_n)/s}}} dy \quad (61)$$

The relative distance from PA to the radial edge of the n^{th} column of vortex sheets are given by the constants, c_n

c_1	$-2R$
c_2	$-(R+R_c)$
c_3	$-(R-R_c)$
c_4	0

The evaluation of the integral begins with the coordinate substitution

$$\cos(\theta_n) = e^{\pi(y+c_n)/s} \quad (62)$$

which transforms the integral into

$$\frac{\Phi_n(PA)}{sw'} = -\frac{1}{\pi} \int_{\theta_n(+a)}^{\theta_n(-a)} d\theta_n = \frac{1}{\pi} [\theta_n(-a) - \theta_n(+a)] \quad (63)$$

Substituting the coordinate transformation back into this result, the new derivation again differs from the classical formula as the potential remains a function of two terms instead of collapsing to a single term. As a result the potential is

$$\frac{\Phi_n(PA)}{sw'} = \frac{1}{\pi} \left[\cos^{-1} \left(e^{\pi(c_n-a)/s} \right) - \cos^{-1} \left(e^{\pi(c_n+a)/s} \right) \right] \quad (64)$$

The root/tip loss function then becomes

$$F = \frac{2}{w's} \Phi(PA) \quad (65)$$

$$F = \sum_{n=1}^4 \frac{2k_n}{\pi} \left[\cos^{-1} \left(e^{\pi(c_n-a)/s} \right) - \cos^{-1} \left(e^{\pi(c_n+a)/s} \right) \right] \quad (66)$$

where the following geometric definitions are used

$$a = (R - y) \quad (67)$$

$$s = \frac{\pi R}{\eta} \quad (68)$$

$$\eta = \frac{N_b \sqrt{(1+\lambda^2)}}{2\lambda} \quad (69)$$

$$f = \eta(1 - \bar{r}) \quad (70)$$

$$\bar{r}_c = R_c/R \quad (71)$$

Final Practical Form of Root/Tip Loss Function

The final practical form of the result for the combined root and tip loss function $F(\bar{r})$ at a given radial station is

$$F = \frac{2}{\pi} \cos^{-1}(e^{-f}) + \sum_{n=1}^3 \frac{k_n}{\pi} \left[\cos^{-1}(e^{-f_n}) - \cos^{-1}(e^{-g_n}) \right] \quad (72)$$

where

$$f = \eta(1 - \bar{r}) \quad (73)$$

and

$$\eta = \frac{N_b \sqrt{1 + \bar{r}^2 \tan^2 \phi}}{2 \bar{r} \tan \phi} \quad (74)$$

with the coefficients within the summation using the local radial station, \bar{r} and the root cutout, \bar{r}_c defined by

n	k_n	f_n	g_n
1	+1	$\eta(3 - \bar{r})$	$\eta(1 + \bar{r})$
2	-2	$\eta(2 - \bar{r} + \bar{r}_c)$	$\eta(\bar{r} + \bar{r}_c)$
3	-2	$\eta(2 - \bar{r} - \bar{r}_c)$	$\eta(\bar{r} - \bar{r}_c)$